JIGGLE: An Active Sensing Framework for Boundary Parameters Estimation in Deformable Surgical Environments

Nikhil Uday Shinde[†] **Xiao Liang**[†] **Fei Liu** **Yutong Zhang**
Florian Richter **Sylvia L. Herbert** **Michael C. Yip**

University of California San Diego [†] Equal contribution.

Abstract: Surgical automation can improve the consistency and accessibility of life-saving procedures. Most surgeries require separating layers of tissue to access the surgical site, and suturing to re-attach incisions. These tasks involve deformable manipulation to safely identify and alter tissue attachment (boundary) topology. Due to poor visual acuity and frequent occlusions, surgeons tend to carefully manipulate the tissue in ways that enable inference of the tissue's attachment points without causing unsafe tearing. In a similar fashion, we propose JIGGLE, a framework for estimation and interactive sensing of unknown boundary parameters in deformable surgical environments. This framework has two key components: (1) a probabilistic estimation to identify the current attachment points, achieved by integrating a differentiable soft-body simulator with an extended Kalman filter (EKF), and (2) an optimization-based active control pipeline that generates actions to maximize information gain of the tissue attachments, while simultaneously minimizing safety costs. The robustness of our estimation approach is demonstrated through experiments with real animal tissue, where we infer sutured attachment points using stereo endoscope observations. We also demonstrate the capabilities of our method in handling complex topological changes such as cutting and suturing.

Keywords: CoRL, Robots, Learning, Active Sensing, Surgical Automation, Deformable Manipulation

1 Introduction

Surgical automation has the potential to improve the accessibility of life-saving procedures in underserved communities. In recent years, the robotics community has made strides in surgical automation with the development of dVRK [1], works like STAR [2], and advancements in the automation of deformable manipulation [3, 4, 5], suturing [6, 7], blood suction [8], cutting [9] and dissection [10].

Deformable manipulation is a significant component of all surgical tasks. Large portions of surgical procedures involve safely cutting tissue to detach regions and access the surgical site, as well as suturing tissue back together. These actions actively change the structure of the surgical scene. A key step towards realizing surgical autonomy is enabling robots to understand and track these changing structures. Many previous works have aimed to take this step solely through 3D scene reconstruction [11, 12, 13, 14]. However, these works are insufficient to enable safe interaction as they fail to estimate and track the change in underlying tissue structures and provide an understanding of how aggressively the tissue is being manipulated.

The key to enabling safer surgical autonomy is an interactive approach to track and control the tissue. Previous approaches like [15] that consider the joint problem of estimation and active sensing are

9th Conference on Robot Learning (CoRL 2025), Seoul, Korea.

limited in the resolution of the attachment regions they can detect. Safety is not considered, and behaviors are limited to hand-tuned motion primitives.Additionally, previous works do not show their results on real tissue data and fail to consider topological changes like cutting and suturing.

In this work, our goal is to realize an interactive approach to estimating, manipulation, and tracking of a deformable thin-shell tissue for safer, more intelligent tissue control. Specifically, we propose the Joint Interactive Guided Gaussian Likelihood Estimation (JIGGLE) method: a novel active sensing framework for estimating boundary attachment points in deformable surgical environments. We leverage a differentiable physics simulator to develop an efficient probabilistic estimation framework for deformable environments with a high degree of freedom (DOF). Our estimation framework relies solely on stereo camera observations which is typically the only available feedback modality during surgery. We demonstrate the robustness of this estimation in real tissue manipulation experiments, as shown in Fig. 1. We take advantage of the probabilistic nature of the estimation framework to build an active sensing pipeline that selects actions to maximize information gain while minimizing a safety cost to avoid tissue tearing. We showcase the complete JIGGLE framework in simulations involving topological changes like cutting and suturing.

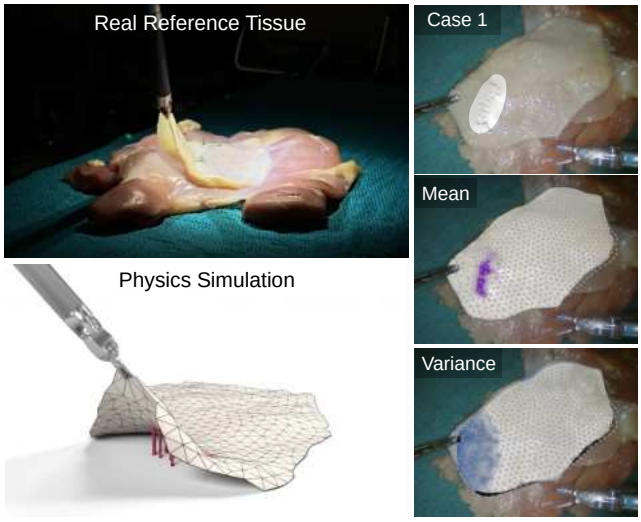

Figure 1: JIGGLE conducts probabilistic estimation of soft tissue attachment points from image data and manipulation of the tissue. The estimated boundary, i.e. the suture locations, are shown in purple. A corresponding confidence metric is shown in blue.

2 Methods

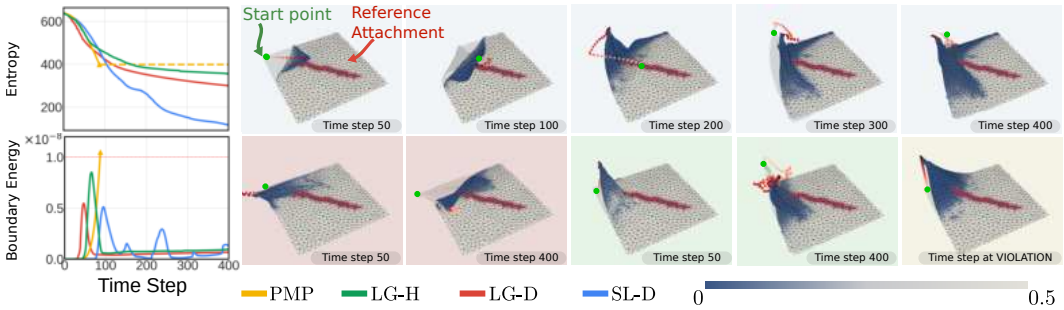

Figure 2: Results from our active sensing experiments with 4 different strategies: SL-D (blue) is our method, LG-H (green) and LG-D (red) are local gradient variations of our method, and PMP (yellow) is a baseline. The red color on the tissue highlights the reference attachment, and the blue shows the confidence, inverse of variance, of the estimated boundary. The dotted line in the boundary energy graph denotes the safety threshold. SL-D achieves more entropy reduction than all other baselines while keeping a safe boundary energy profile. In comparison, local controllers LG-H and LG-D get trapped in local minima, resulting in higher entropy. PMP results in quick safety violations. Additional active sensing results can be found in Fig. 7 of the appendix.

Problem Statement: In this paper we consider a deformable thin shell tissue $\mathcal{T}$ represented by a mesh with n particles with positions $\mathbf{x}_t = [\mathbf{x}_t^1 \dots \mathbf{x}_t^n] \in \mathbb{R}^{n\times 3}$ at time t. A subset of the tissue $\mathcal{T}_b \subseteq \mathcal{T}$ is attached to the environment by boundary constraints of varying strength parameterized by $\mathbf{b}_t = [\mathbf{b}_n^1 \dots \mathbf{b}_t^n] \in \mathbb{R}^{n\times 1}$. The tissue is controlled by moving a fixed point on the tissue with actions $u_t \in \mathbb{R}^3$. Our goal for the estimation task is to estimate the true boundary constraints $\mathbf{b}^*$ given observations of a real reference tissue $\mathcal{T}_{\text{ref}}$. For active sensing, we aim to maximize information gain and find the best actions to estimate $\mathbf{b}^*$.

Estimation: To solve the above problem statement we represent **Extended Position-based Dynamics (XPBD)** [16]. We control the tissue with actions u_t that specify the position of an infinite-mass virtual control particle that is connected to a local neighborhood of points on the tissue mesh. We formulate our boundary constraints as zero resting length spring attachments between each tissue particle and infinite-mass virtual particles that are fixed to the tissue particle's initial resting positions $\mathbf{x}_0 = [\mathbf{x}_0^1 \dots \mathbf{x}_0^n]$.

We propose a probabilistic estimation framework to track boundary constraint distributions, $\mathbf{b}_t$, over the true boundary parameters. The differentiability of the XPBD simulation allows us to locally linearize the tissue model. This in conjunction with a multivariate Gaussian representation of $\mathbf{b}_t \sim \mathcal{N}(\widehat{\mathbf{b}}_t, \Sigma_t)$ allows us to easily track $\mathbf{b}_t$ with an extended Kalman Filter (EKF) formulation. The motion model of our EKF describes the change in the boundary estimate $\mathbf{b}_t$ between the time steps. We use $\delta\mathbf{b}_t \in \mathbb{R}^n$ to represent topology-changing actions, such as suturing or cutting, that directly modify the boundary parameters.

$$\begin{aligned} \mathbf{b}_{t+1} &= m(\mathbf{b}_t, \delta\mathbf{b}_t, w_t) = \mathbf{b}_t + \delta\mathbf{b}_t + w_t \\ w_t &\sim \mathcal{N}(0, W_t) \end{aligned} \tag{1}$$

During topology changing actions $\delta\mathbf{b}_t$ is non-zero with W_t having larger covariance values near the modified regions.

As the boundary parameters are not directly visible, we observe them indirectly through the tissue x_t^{ref}:

$$\begin{aligned} \mathbf{x}_{t+1} &= h(\mathbf{b}_{t+1}, \mathbf{x}_t^{\text{ref}}, u_t, v_t) = f(\mathbf{x}_t^{\text{ref}}, u_t, \mathbf{b}_{t+1}) + v_{t+1} \\ v_{t+1} &\sim \mathcal{N}(0, V_{t+1}) \end{aligned} \tag{2}$$

Here, we initialize the XPBD simulation, f, with the last observed tissue state, x_t^{ref}, and forward simulate with the belief the boundary constraints from the motion model.

Using equations 1 and 2 we can track the changes to the boundary parameter belief, represented by $\widehat{\mathbf{b}}_t$ and $\mathbf{\Sigma}_t$.

Prediction :

$$\widehat{\mathbf{b}}_{t+1|t} = \widehat{\mathbf{b}}_{t|t} + \delta\mathbf{b}_t, \;\; \mathbf{\Sigma}_{t+1|t} = \mathbf{\Sigma}_{t|t} + W_t \tag{3}$$

Update :

$$\begin{aligned} \widehat{\mathbf{b}}_{t+1|t+1} &= \widehat{\mathbf{b}}_{t+1|t} + K_{t+1}\tilde{\mathbf{y}}_{t+1} \\ \mathbf{\Sigma}_{t+1|t+1} &= (I - K_{t+1}J_{t+1})\mathbf{\Sigma}_{t+1|t} \end{aligned} \tag{4}$$

where the observation residual $\tilde{\mathbf{y}}_{t+1}$, and the Kalman gain K_{t+1} are given by:

$$\begin{aligned} \tilde{\mathbf{y}}_{t+1} &= \mathbf{x}_{t+1}^{\text{ref}} - h(\widehat{\mathbf{b}}_{t+1|t}, \mathbf{x}_t^{\text{ref}}, u_t, v_t) \\ K_{t+1} &= \mathbf{\Sigma}_{t+1|t} J_{t+1}^\top S_{t+1}^{-1} \end{aligned} \tag{5}$$

with the residual covariance S_{t+1}, the observation Jacobians J_{t+1}, and covariance Jacobians R_{t+1} as:

$$\begin{aligned} S_{t+1} &= J_{t+1}\mathbf{\Sigma}_{t+1|t}J_{t+1}^\top + R_{t+1}V_{t+1}R_{t+1}^\top \\ R_{t+1} &= \left.\frac{\partial h}{\partial v}\right|_{\widehat{\mathbf{b}}_{t+1|t}} = I \\ J_{t+1} &= \left.\frac{\partial h}{\partial \mathbf{b}}\right|_{\widehat{\mathbf{b}}_{t+1|t}} = \left.\frac{\partial f(\mathbf{x}_t^{\text{ref}}, u_t, \mathbf{b}_{t+1})}{\partial \mathbf{b}}\right|_{\widehat{\mathbf{b}}_{t+1|t}} \end{aligned} \tag{6}$$

Table 1: Comparison of boundary estimation accuracy after 4 grasp sequences. Results demonstrate our method outperforms the baseline Adam Optimizer.

	PCD ↑		PUG ↑	
Cases	Adam	Ours	Adam	Ours
Arc	82.1	100	59.3	87.1
Line	85.7	100	40.0	43.3
Line-dot	68.0	96.0	34.7	48.9
Arc-line	83.8	97.3	51.8	65.5
U-shape	87.3	97.5	52.9	76.0

Here, $f(\mathbf{x}_t^{\text{ref}}, \widehat{\mathbf{b}}_{t+1|t}, u_t)$ outputs the expected tissue surface after using the XPBD simulator to forward simulate one timestep with action u_t, using the mean of the current estimated boundary belief, $\widehat{\mathbf{b}}_{t+1|t}$. To enhance the robustness of our estimation, we modify the EKF to use k uniform samples of previous observations up until the last topology changing action. We use the multiple shooting method to encode previous observations [17]; this approach samples from previously observed trajectories, forward simulates from those samples using the current belief and penalizes the deviation of predicted particle states from the reference observations. To get accurate observations of the tissue state, x_t^{ref}, for real world experiments, we introduce an observation-matching condition into the XPBD simulation's iterative constraint solving procedure, similar to [18]. As this condition uses the current boundary constraint estimate, $\mathbf{b}_t$, we combine the EKF update and state estimation into one joint estimation problem where both are iteratively estimated.

Active Sensing: For the active sensing problem, we want to solve for actions that minimize the entropy of the boundary constraint belief distribution, $\mathbf{b}_t$, while minimizing the boundary energy to prevent the tissue from experiencing unsafe forces. In place of the computationally complex entropy minimization objective we introduce a heuristic to maximize $\mathcal{D}$: Uncertainty-Weighted Displacement (UWD).

$$\mathcal{D}(\mathbf{x}_t^{\text{ref}}, u_t, \widehat{\mathbf{b}}_t) = \widehat{\Delta \mathbf{x}_{t+1}} \cdot \mathbf{\Sigma}_t \tag{7}$$

$$\begin{aligned} \mathbf{x}_{t+1} &= f\left(\mathbf{x}_t^{\text{ref}}, u_t, \widehat{\mathbf{b}}_{t+1|t}\right), \ \Delta \mathbf{x}_{t+1} = \mathbf{x}_{t+1} - \mathbf{x}_0 \\ \widehat{\Delta \mathbf{x}_{t+1}} &= \sum_i^n \mathbf{e}_i \mathbf{e}_i^\top \otimes [\Delta \mathbf{x}_{t+1}]_i. \end{aligned} \tag{8}$$

Here e_i is the ith standard basis vector and $\otimes$ is the kronecker product. This effectively maximizes information gain by encouraging more displacement in regions that are more uncertain as weighted by Σ_t. We prevent unsafe actions by adding objectives to minimize the energy on the tissue's boundary constraints and limit the range of the actions.

Optimizing the above objectives for the best actions using a local gradient based controller suffers from local minima as well as vanishing gradient issues. Evaluating a multi-step trajectory also imposes computational challenges. To address these challenges we introduce a sampling-based large step controller. We first uniformly sample several large-step control actions. We refine these actions through gradient step updates with respect to the optimization objectives. We then select the action that best optimizes our objective before taking a small step in its direction and re-planning. We encourage smoothness by carrying over the top 10 samples across each sampling iteration.

3 Experimental Results

We evaluate our estimation method in simulation over 5 different environments. We repeat 4 grasp sequences on the 4 corners of the tissue while running our estimation framework. We record the percentage of correct detections of attachment points (PCD) and the percentage of the uncovered ground truth (PUG). Table 1 summarizes our results with our method performing the baseline of updating the boundary parameters using gradient updates: "adam". The environments and experiments are visualized in Fig. 8 and 9 in the appendix.

Table 2: Real world estimation results. The number after the metrics corresponds to the dilation factor applied.

	PCD ↑	PCD-1	PCD-2	PUG ↑	PUG-1	PUG-2
Case1-BANet	0	0	0	0	0	0
Case1-Adam	46.2	**84.6**	84.6	54.5	100.0	100.0
Case1-Ours	**47.4**	84.2	**89.5**	**81.8**	100.0	100.0
Case1-Ours-σ=0.1	60	93.3	100	81.8	100.0	100.0
Case2-BANet	0	0	7.1	0	0	7.5
Case2-Adam	0.0	2.1	10.4	0.0	2.5	17.5
Case2-Ours	**33.3**	**83.3**	**100.0**	**5.0**	**27.5**	**37.5**
Case2-Ours-σ=0.1	40.0	100	100.0	11.1	55.6	72.2

We also evaluate our estimation framework in a real world experiment shown in Fig. 1 and Fig. 10 in the appendix. We create boundary constraints by suturing chicken skin to a chicken thigh. We are able to successfully recover the tissue's boundary constraints from endoscopic camera observations of manipulating the tissue using tweezers. We compare the PCD and PUG of our method, "adam" baseline and BANet [19] in Table 2. Visual comparisons can be found in Fig. 11

To evaluate active sensing, we compare four different variants of our proposed framework:

1. **LG-H**: Local gradient-based action, minimizing entropy. Only refines actions with local gradient based updates.
2. **LG-D**: Local gradient-based, maximizing displacement
3. **SL-D**: Our proposed method
4. **PMP**: Predefined motion primitives: An exhaustive search to minimize entropy over motion primitives of $(\pm x, \pm y, \pm z)$. [15]

Our method, SL-D, consistently achieves greater entropy reduction while keeping a safe boundary energy profile. Results of this are shown in Fig. 2. Using motion model m, our framework can also handle topological changes, and be used to estimate the success of suturing or cutting. Examples of these procedures are shown Fig. 12 and 13 in the appendix.

4 Conclusion

In this paper we proposed a novel framework for active sensing and boundary parameter estimation in deformable surgical environments. We demonstrated the estimation capabilities of our method in both simulation and real world experiments. Our active sensing experiments showcased our method's ability to manipulate the tissue to maximize information gain while respecting safety constraints.

5 Limitations

While our work introduces a novel approach for boundary parameter estimation in deformable environments, we demonstrate its effectiveness primarily on thin-shell tissue models. Extending this framework to more complex three-dimensional deformable structures remains an important direction for future work. Such scenarios introduce additional challenges, including self-occlusion, where portions of the tissue obscure critical features and limit the quality of observations available to the EKF. Furthermore, three-dimensional structures may exhibit heterogeneous internal properties, making it difficult for observations from a single viewpoint to fully capture the boundary conditions throughout the tissue.

Acknowledgments

References

[1] P. Kazanzides, Z. Chen, A. Deguet, G. S. Fischer, R. H. Taylor, and S. P. DiMaio. An open-source research kit for the da vinci® surgical system. In *2014 IEEE International Conference on Robotics and Automation (ICRA)*, pages 6434–6439, 2014. doi:10.1109/ICRA.2014.6907809.

[2] A. Shademan, R. S. Decker, J. D. Opfermann, S. Leonard, A. Krieger, and P. C. W. Kim. Supervised autonomous robotic soft tissue surgery. *Science Translational Medicine*, 8(337):337ra64–337ra64, 2016. doi:10.1126/scitranslmed.aad9398. URL https://www.science.org/doi/abs/10.1126/scitranslmed.aad9398.

[3] Z. Hu, T. Han, P. Sun, J. Pan, and D. Manocha. 3-d deformable object manipulation using deep neural networks. *IEEE Robotics and Automation Letters*, 4(4):4255–4261, 2019.

[4] B. P. Murphy and F. Alambeigi. A surgical robotic framework for safe and autonomous data-driven learning and manipulation of an unknown deformable tissue with an integrated critical space. *Journal of Medical Robotics Research*, 8(01n02):2340001, 2023.

[5] B. Thach, B. Y. Cho, A. Kuntz, and T. Hermans. Learning visual shape control of novel 3d deformable objects from partial-view point clouds. In *2022 International Conference on Robotics and Automation (ICRA)*, pages 8274–8281. IEEE, 2022.

[6] Z. Chiu, A. Z. Liao, F. Richter, B. Johnson, and M. C. Yip. Markerless suture needle 6d pose tracking with robust uncertainty estimation for autonomous minimally invasive robotic surgery. *CoRR*, abs/2109.12722, 2021. URL https://arxiv.org/abs/2109.12722.

[7] H. Saeidi, H. N. D. Le, J. D. Opfermann, S. Leonard, A. Kim, M. H. Hsieh, J. U. Kang, and A. Krieger. Autonomous laparoscopic robotic suturing with a novel actuated suturing tool and 3d endoscope. In *2019 International Conference on Robotics and Automation (ICRA)*, pages 1541–1547, 2019. doi:10.1109/ICRA.2019.8794306.

[8] F. Richter, S. Shen, F. Liu, J. Huang, E. K. Funk, R. K. Orosco, and M. C. Yip. Autonomous robotic suction to clear the surgical field for hemostasis using image-based blood flow detection. *IEEE Robotics and Automation Letters*, 6(2):1383–1390, 2021. doi:10.1109/LRA.2021.3056057.

[9] B. Thananjeyan, A. Garg, S. Krishnan, C. Chen, L. Miller, and K. Goldberg. Multilateral surgical pattern cutting in 2d orthotropic gauze with deep reinforcement learning policies for tensioning. In *2017 IEEE International Conference on Robotics and Automation (ICRA)*, pages 2371–2378, 2017. doi:10.1109/ICRA.2017.7989275.

[10] J. Ge, M. Kam, J. D. Opfermann, H. Saeidi, S. Leonard, L. J. Mady, M. J. Schnermann, and A. Krieger. Autonomous system for tumor resection (astr) - dual-arm robotic midline partial glossectomy. *IEEE Robotics and Automation Letters*, 9(2):1166–1173, 2024. doi:10.1109/LRA.2023.3341773.

[11] Y. Li, F. Richter, J. Lu, E. K. Funk, R. K. Orosco, J. Zhu, and M. C. Yip. Super: A surgical perception framework for endoscopic tissue manipulation with surgical robotics. *IEEE Robotics and Automation Letters*, 5(2):2294–2301, Apr. 2020. ISSN 2377-3774. doi:10.1109/lra.2020.2970659. URL http://dx.doi.org/10.1109/LRA.2020.2970659.

[12] S. Lin, A. J. Miao, J. Lu, S. Yu, Z.-Y. Chiu, F. Richter, and M. C. Yip. Semantic-super: A semantic-aware surgical perception framework for endoscopic tissue identification, reconstruction, and tracking. In *2023 IEEE International Conference on Robotics and Automation (ICRA)*, pages 4739–4746, 2023. doi:10.1109/ICRA48891.2023.10160746.

[13] Y. Long, Z. Li, C. H. Yee, C. Ng, R. H. Taylor, M. Unberath, and Q. Dou. E-DSSR: efficient dynamic surgical scene reconstruction with transformer-based stereoscopic depth perception. *CoRR*, abs/2107.00229, 2021. URL https://arxiv.org/abs/2107.00229.

[14] Y. Wang, Y. Long, S. H. Fan, and Q. Dou. Neural rendering for stereo 3d reconstruction of deformable tissues in robotic surgery. In *International conference on medical image computing and computer-assisted intervention*, pages 431–441. Springer, 2022.

[15] P. Boonvisut and M. C. Çavuşoğlu. Identification and active exploration of deformable object boundary constraints through robotic manipulation. *The International journal of robotics research*, 33(11):1446–1461, 2014.

[16] M. Macklin, M. Müller, and N. Chentanez. Xpbd: position-based simulation of compliant constrained dynamics. In *Proceedings of the 9th International Conference on Motion in Games*, pages 49–54, 2016.

[17] E. Heiden, C. E. Denniston, D. Millard, F. Ramos, and G. S. Sukhatme. Probabilistic inference of simulation parameters via parallel differentiable simulation. In *2022 International Conference on Robotics and Automation (ICRA)*, pages 3638–3645. IEEE, 2022.

[18] X. Liang, F. Liu, Y. Zhang, Y. Li, S. Lin, and M. Yip. Real-to-sim deformable object manipulation: Optimizing physics models with residual mappings for robotic surgery. *arXiv preprint arXiv:2309.11656*, 2023.

[19] E. Tagliabue, D. Dall'Alba, M. Pfeiffer, M. Piccinelli, R. Marin, U. Castellani, S. Speidel, and P. Fiorini. Data-driven intra-operative estimation of anatomical attachments for autonomous tissue dissection. *IEEE Robotics and Automation Letters*, 6(2):1856–1863, 2021. doi:10.1109/LRA.2021.3060655.

6 Appendix

6.1 Relationship Between Uncertainty-Weighted Displacement (UWD) and Boundary Entropy

In this section we present the following proposition, and provide a proof tying the relationship between the UWD, i.e., displacement, $\mathcal{D}$, of the tissue particles from their initial position, and the reduction in boundary entropy $\mathcal{H}(\mathbf{b_{t+1}})$ at the next timestep $t+1$.

The active sensing objective of maximizing the uncertainty-weighted deformation displacement, i.e., $\mathcal{D}$ in Eq. 7, is designed to decrease the entropy $\mathcal{H}(\mathbf{b}_{t+1})$ of boundary estimation and uncover more unknown information. That is,

$$\min \mathcal{H}(\mathbf{b}_{t+1}) \propto \max \mathcal{D} \tag{9}$$

To prove it, we first establish a connection to entropy, $\mathcal{H}$, via the observation Jacobian $J_{t+1} = \frac{\partial h}{\partial \mathbf{b}}$, defined in Eq. 6 of the EKF equations in section 6.1.1. Second, we derive the relationship between the Jacobian J and the tissue displacement in section 6.1.2. Third, we combine these results to show proposition 1 in section 6.1.3.

6.1.1 Boundary Entropy Regarding the Observation Jacobian

As defined in Eq. **??**, it is evident that the entropy $\mathcal{H}(\mathbf{b}_{t+1})$ is directly proportional to the determinant of the covariance matrix outputted by the Extended Kalman Filter (EKF) estimator. Since $\mathbf{\Sigma}_{t|t}, W_t, V_t$ are all positive semi-definite covariance matrices, they allow the following factorization:

$$\mathbf{\Sigma}_{t+1|t} = \mathbf{\Sigma}_{t|t} + W_t = \mathbf{\Sigma}^{\frac{1}{2}}\mathbf{\Sigma}^{\frac{1}{2}} \tag{10}$$

Combining this fact with the Extended Kalman Filter (EKF) equations, as defined in Eq. 3 and 4, and for the sake of simplicity, neglecting the subscripts of observation Jacobian J_{t+1} and Kalman gain K_{t+1}, we obtain:

$$\begin{aligned}
\mathcal{H}(\mathbf{b}_{t+1}) &\propto \left|\mathbf{\Sigma}_{t+1|t+1}\right| \\
&\propto \left|\Big(I - KJ\Big)\mathbf{\Sigma}_{t+1|t}\right| \\
&\propto \left|\Big(I - \mathbf{\Sigma}_{t+1|t}J^\top\left[J\mathbf{\Sigma}_{t+1|t}J^\top + V_t\right]^{-1}J\Big)\mathbf{\Sigma}_{t+1|t}\right| \\
&\propto \left|\Big(I - \mathbf{\Sigma}^{\frac{1}{2}}\mathbf{\Sigma}^{\frac{1}{2}}J^\top\left[J\mathbf{\Sigma}^{\frac{1}{2}}\mathbf{\Sigma}^{\frac{1}{2}}J^\top + V_t\right]^{-1}J\Big)\mathbf{\Sigma}^{\frac{1}{2}}\mathbf{\Sigma}^{\frac{1}{2}}\right| \\
&\propto \left|\Big(I - \mathbf{\Sigma}^{\frac{1}{2}}J^\top\left[J\mathbf{\Sigma}^{\frac{1}{2}}\mathbf{\Sigma}^{\frac{1}{2}}J^\top + V_t\right]^{-1}J\mathbf{\Sigma}^{\frac{1}{2}}\Big)\right|\left|\mathbf{\Sigma}^{\frac{1}{2}}\mathbf{\Sigma}^{\frac{1}{2}}\right|
\end{aligned} \tag{11}$$

Denoting $\mathsf{A} = J\mathbf{\Sigma}^{\frac{1}{2}}$ and $\mathbf{\Sigma}_{t+1|t} = \mathbf{\Sigma} = \mathbf{\Sigma}^{\frac{1}{2}}\mathbf{\Sigma}^{\frac{1}{2}}$, we can perform singular value decomposition (SVD) where D is a matrix with singular values λ_i on its diagonal, $UU^T = U^TU = I$, and $QQ^T = Q^TQ = I$.

$$\mathsf{A} = J\mathbf{\Sigma}^{\frac{1}{2}} = UDQ^\top \tag{12}$$

For simplification and to maintain a straightforward representation of observation uncertainty, we assume $V_t = \alpha I$, with α denotes the maximum expected observation noise variance. This diagonal covariance matrix implies that the observation noise is isotropic and of uniform magnitude across

different dimension. Substituting them into Eq. 11, we get:

$$
\begin{aligned}
\mathcal{H}(\mathbf{b}_{t+1}) \propto & \\
& \propto \left| I - \mathsf{A}^\top \left[\mathsf{A}\mathsf{A}^\top + \alpha I\right]^{-1} \mathsf{A} \right| \left| \mathbf{\Sigma} \right| \\
& \propto \left| QQ^\top - QD^\top U^\top \left[UDD^\top U^\top + \alpha I\right]^{-1} UDQ^\top \right| \left| \mathbf{\Sigma} \right| \\
& \propto \left| Q \right| \left| I - D^\top U^\top \left[UDD^\top U^\top + \alpha I\right]^{-1} UD \right| \left| Q^\top \right| \left| \mathbf{\Sigma} \right| \\
& \propto \left| Q \right| \left| Q^\top \right| \left| I - D^\top U^\top \left[UDD^\top U^\top + \alpha I\right]^{-1} UD \right| \left| \mathbf{\Sigma} \right| \\
& \propto \left| I - D^\top U^\top \left[UDD^\top U^\top + \alpha I\right]^{-1} UD \right| \left| \mathbf{\Sigma} \right| \\
& \propto \left| I - D^\top U^\top \left[UDD^\top U^\top + \alpha UU^\top\right]^{-1} UD \right| \left| \mathbf{\Sigma} \right| \\
& \propto \left| I - D^\top U^\top U \left[DD^\top + \alpha I\right]^{-1} U^\top UD \right| \left| \mathbf{\Sigma} \right| \\
& \propto \left| (I - D^\top (DD^\top + \alpha I)^{-1} D) \right| \left| \mathbf{\Sigma} \right| \\
& \propto |\mathbf{\Sigma}| \prod_i^N \left(1 - \frac{{\lambda_i}^2}{{\lambda_i}^2 + \alpha}\right)
\end{aligned}
\tag{13}
$$

In Eq. 13 and Eq. 10, the only term influenced by our control actions at time t is the observation Jacobian J, as $\mathbf{\Sigma}$ only depends on the estimation from the previous step. These equations show that selecting J in a manner that increases the magnitudes of the singular values $||\lambda_i||_2$ of $J\mathbf{\Sigma}^{\frac{1}{2}}$ will result in a reduction of the entropy within the belief distribution.

After establishing the correlation between the Jacobian and entropy reduction, we need to link the uncertainty-weighted displacement (UWD) of particles to the Jacobian. We must identify the choices of UWD that lead to entropy reduction. Demonstrating these connections will validate that our Proposition 9.

6.1.2 Observation Jacobian Regarding the Uncertainty-Weighted Displacement (UWD)

To link the Jacobian, J, at the next timestep $t+1$, to displacement we derive an analytical form of J. To derive the exact form of observation Jacobian, we illustrate the simulated mesh with a simplified graph in Fig. 3. Hence, we partition our whole tissue state representation $\mathbf{x} = \{\mathbf{x}^{\mathsf{B}}_{t+1}, \mathbf{x}^{\mathsf{U}}_{t+1}\}$ into particles related to boundary constraints $\mathbf{x}^{\mathsf{B}}_{t+1}$ and other particles denoted as $\mathbf{x}^{\mathsf{U}}_{t+1}$. Of the n total particles, we assume that there are m particles in $\mathbf{x}^{\mathsf{B}}_{t+1}$ and q particles in $\mathbf{x}^{\mathsf{U}}_{t+1}$ such that $m + q = n$. From the definition in Eq. **??**, the XPBD simulation involves minimizing the total energy potential of constraints:

$$
\arg\min_{\mathbf{x}} \mathcal{U}(\mathbf{x}, \mathbf{b}) = \arg\min_{\mathbf{x}} \mathcal{U}_1(\mathbf{x}^{\mathsf{B}}_{t+1}, \mathbf{b}) + \mathcal{U}_2(\mathbf{x}^{\mathsf{U}}_{t+1}, \mathbf{x}^{\mathsf{B}}_{t+1}) \tag{14}
$$

where the first term, $\mathcal{U}_1(\mathbf{x}^{\mathsf{U}}_{t+1}, \mathbf{x}^{\mathsf{B}}_{t+1})$, representing the energy only related to the current boundary constraints, $\mathbf{b}$ and $\mathcal{U}_2(\mathbf{x}^{\mathsf{U}}_{t+1}, \mathbf{x}^{\mathsf{B}}_{t+1})$ denotes the energy term associated with both $\mathbf{x}^{\mathsf{U}}_{t+1}$ and $\mathbf{x}^{\mathsf{B}}_{t+1}$. In our XPBD simulator, all defined constraints are distance constraints between particles. For the boundary energy, we are able to write:

$$
\begin{aligned}
\mathcal{U}_1(\mathbf{x}^{\mathsf{B}}_{t+1}, \mathbf{b}) &= \frac{1}{2}\mathbf{C}^\top(\mathbf{x}^{\mathsf{B}}_{t+1})\mathtt{diag}(\mathbf{b})\mathbf{C}(\mathbf{x}^{\mathsf{B}}_{t+1}) \\
&= \frac{1}{2}\sum_{i=1}^{m} b_i \left(\mathbf{x}^{\mathsf{B},i}_{t+1} - {\mathbf{x}^{\mathsf{B},i}_0}_2 - d^{\mathsf{B},i}_0\right)^2
\end{aligned}
\tag{15}
$$

$\mathbf{b} \in \mathbb{R}^m$ where b_i is the stiffness of the i-th boundary spring, of the total m springs. ${\mathbf{x}^{\mathsf{B}}_{t+1}}^{,i} - \mathbf{x}^{\mathsf{B},i}_0$ is the displacement of particle i related to the boundary constraint from time 0 to the next time step $t+1$. $d^{\mathsf{B},i}_0$ is the length of the boundary spring associated with particle i at rest time, $t = 0$. For our

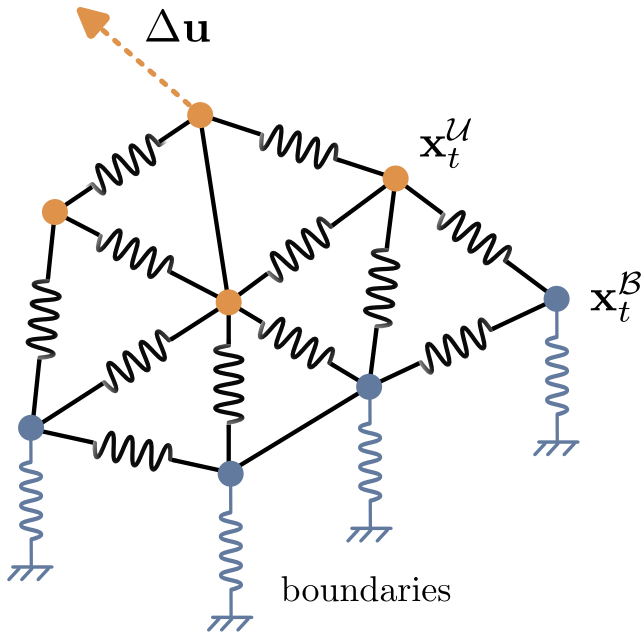

Figure 3: This figure shows a simplified model of the XPBD simulation. The particles shown in blue, $\mathbf{x}_{t+1}^{\mathsf{B}}$, are related to the boundary constraints. We are trying to estimate the boundary parameters associated with the boundary constraints on these particles. The remaining particles are shown in orange, $\mathbf{x}_{t+1}^{\mathsf{U}}$. The virtual particle u is used to apply control on the tissue. All constraints are implemented as set distance constraints and are depicted using springs with different springs constants set according to the associated constraint.

work, we consider a zero length spring at rest, $d_0^{\mathsf{B},i} = 0, \forall i$, for all boundary springs. Similarly, we describe the rest of spring potential energy by:

$$\begin{aligned} \mathcal{U}_2(\mathbf{x}_{t+1}^{\mathsf{U}}, \mathbf{x}_{t+1}^{\mathsf{B}}) &= \frac{1}{2}\mathbf{C}^\top(\mathbf{x}_{t+1}^{\mathsf{U}}, \mathbf{x}_{t+1}^{\mathsf{B}})\mathtt{diag}(\mathbf{k})\mathbf{C}(\mathbf{x}_{t+1}^{\mathsf{U}}, \mathbf{x}_{t+1}^{\mathsf{B}}) \\ &= \frac{1}{2}\sum_{j=1}^{s} k_j \left(\mathbf{x}_{t+1}^{j,1} - \mathbf{x}_{t+1}^{j,2} - d_0^{1,2,j}\right)^2 \end{aligned} \tag{16}$$

where $\mathbf{x}_{t+1}^{j,1}, \mathbf{x}_{t+1}^{j,2} \in \{\mathbf{x}_{t+1}^{\mathsf{B}} \cup \mathbf{x}_{t+1}^{\mathsf{U}}\}$ are a pair of two particles connected by the j-th spring within the simulated mesh. $d_0^{1,2,j}$ is the distance of that j-th spring constraint between particle 1 and 2 at rest, at time $t = 0$. Using this, we are able to define the matrices $\mathbf{L} \in \mathbb{R}^{3n\times 3n}$ and $\mathbf{P} \in \mathbb{R}^{3n\times 3s}$ as follows:

$$\begin{aligned} \mathbf{L} &= \left(\sum_{j=1}^{s} k_j \mathbf{A}^j \mathbf{A}^{j,\top}\right) \otimes \mathbf{I}_3 \\ \mathbf{P} &= \left(\sum_{j=1}^{s} k_j \mathbf{A}^j \mathbf{S}^{j,\top}\right) \otimes \mathbf{I}_3 \\ \mathbf{d} &= \frac{\mathbf{x}_0^{j,1} - \mathbf{x}_0^{j,2}}{\mathbf{x}_0^{j,1} - \mathbf{x}_0^{j,2}}_2 d_0^{1,2,j} \end{aligned} \tag{17}$$

Here, $\mathbf{A}_j \in \mathbb{R}^n$ is the connectivity vector of the j-th spring, i.e., $\mathbf{A}^{j,1} = 1$, $\mathbf{A}^{j,2} = -1$, and zero otherwise. $(j, 1)$ and $(j, 2)$ denote the indices of the first and second particle, respectively, associated with the j-th spring constraint. $\mathbf{S}^j \in \mathbb{R}^s$ is j-th spring indicator, i.e., $\mathbf{S}^j = \mathbf{1}_s$, s is the number of non-boundary related springs or edges, and $\otimes$ denotes Kronecker product. $\mathbf{d}$ can be interpreted as a spring in the rest pose, at time $t = 0$, that is rotated in a specific direction, effectively behaving like

a constant. Eq. 18 can be re-factorized into:

$$\mathcal{U}_2(\mathbf{x}^{\mathsf{U}}_{t+1}, \mathbf{x}^{\mathsf{B}}_{t+1}) = \frac{1}{2}\mathbf{x}^\top \mathbf{L}\mathbf{x} - \mathbf{x}^\top \mathbf{P}\mathbf{d} \tag{18}$$

The solution to the minimization function described in Eq. 14 can be regarded to satisfy:

$$\nabla_{\mathbf{x}}\mathcal{U}(\mathbf{x}, \mathbf{b}) = \nabla_{\mathbf{x}}\mathcal{U}_1(\mathbf{x}^{\mathsf{B}}_{t+1}, \mathbf{b}) + \nabla_{\mathbf{x}}\mathcal{U}_2(\mathbf{x}^{\mathsf{U}}_{t+1}, \mathbf{x}^{\mathsf{B}}_{t+1}) = 0 \tag{19}$$

Before moving forward we explicitly clarify the structure of our state x. Assuming a system with 2 particles, $\mathbf{x}^{\mathsf{B}}_{t+1} = [\mathbf{x}^{\mathsf{B}}_{t+1}[0], \mathbf{x}^{\mathsf{B}}_{t+1}[1], \mathbf{x}^{\mathsf{B}}_{t+1}[2]]^\top$ is the single particle related to boundary constraints and $\mathbf{x}^{\mathsf{U}}_{t+1} = [\mathbf{x}^{\mathsf{U}}_{t+1}[0], \mathbf{x}^{\mathsf{U}}_{t+1}[1], \mathbf{x}^{\mathsf{U}}_{t+1}[2]]^\top$ is the single other particle. $\mathbf{x}$ is a flattened joint state of the 2 particles in the following form: $\mathbf{x} = [\mathbf{x}^{\mathsf{B}}_{t+1}[0], \mathbf{x}^{\mathsf{B}}_{t+1}[1], \mathbf{x}^{\mathsf{B}}_{t+1}[2], \mathbf{x}^{\mathsf{U}}_{t+1}[0], \mathbf{x}^{\mathsf{U}}_{t+1}[1], \mathbf{x}^{\mathsf{U}}_{t+1}[2]]^\top$. For multiple particles we follow a similar structure where the flattened form of the boundary related particles is stacked above the flattened form of the other particles. This gives us: $\mathbf{x}^{\mathsf{B}}_{t+1} \in \mathbb{R}^{3m}$, $\mathbf{x}^{\mathsf{U}}_{t+1} \in \mathbb{R}^{3q}$, $\mathbf{x} \in \mathbb{R}^{3n}$

[Implicit-Function Theorem] Considering the solution function defined in Eq. 19,

$$\mathcal{L}(\mathbf{x}^*, \mathbf{b}) = \nabla_{\mathbf{x}}\mathcal{U}(\mathbf{x}^*, \mathbf{b}) = 0 \tag{20}$$

with x^* defined as an equilibrium point, the sensitivities of the solution with respect to the parameter b can be can be computed as:

$$\frac{\partial \mathbf{x}^*}{\partial \mathbf{b}} = -\left(\frac{\partial \mathcal{L}}{\partial \mathbf{x}}\right)^{-1} \frac{\partial \mathcal{L}}{\partial \mathbf{b}} \tag{21}$$

In our EKF formulation, the observation Jacobian is given by

$$J = \frac{\partial h}{\partial \mathbf{b}} = \frac{\partial f(\mathbf{x}^{\text{ref}}, u, \mathbf{b})}{\partial \mathbf{b}} = \frac{\partial \mathbf{x}}{\partial \mathbf{b}} \tag{22}$$

Combining it with the implicit-function theorem in Eq. 21, we obtain the Jacobian as,

$$\begin{aligned} J &= -\left(\frac{\partial \mathcal{L}}{\partial \mathbf{x}}\right)^{-1} \frac{\partial \mathcal{L}}{\partial \mathbf{b}} = -\left(\frac{\partial \nabla_{\mathbf{x}}\mathcal{U}}{\partial \mathbf{x}}\right)^{-1} \frac{\partial \nabla_{\mathbf{x}}\mathcal{U}}{\partial \mathbf{b}} \\ &= -\left(\frac{\partial^2 \mathcal{U}}{\partial \mathbf{x}\partial \mathbf{x}^\top}\right)^{-1} \frac{\partial^2 \mathcal{U}}{\partial \mathbf{b}\partial \mathbf{x}^\top} \end{aligned} \tag{23}$$

Given $\mathbf{x} = \{\mathbf{x}^{\mathsf{B}}_{t+1}, \mathbf{x}^{\mathsf{U}}_{t+1}\}$, we can computer the following gradients as,

$$\begin{aligned} \frac{\partial \mathcal{U}_1}{\partial \mathbf{x}} &= \begin{bmatrix} \Delta \mathbf{x}^{\mathsf{B}}_{t+1}{}^\top \mathtt{diag}(\mathbf{b}) & \mathbf{0} \end{bmatrix} \in \mathbb{R}^{3n\times 1} \\ \frac{\partial \mathcal{U}_2}{\partial \mathbf{x}} &= \begin{bmatrix} \mathbf{x}^{\mathsf{B}}_{t+1}{}^\top \mathbf{L}_{\mathsf{BB}} + \mathbf{x}^{\mathsf{U}}_{t+1}{}^\top \mathbf{L}_{\mathsf{UB}} \\ \mathbf{x}^{\mathsf{U}}_{t+1}{}^\top \mathbf{L}_{\mathsf{UU}} + \mathbf{x}^{\mathsf{B}}_{t+1}{}^\top \mathbf{L}_{\mathsf{BU}} \end{bmatrix}^\top \\ &\quad - (\mathbf{P}\mathbf{d})^\top \\ &\in \mathbb{R}^{3n\times 1} \\ \frac{\partial^2 \mathcal{U}_1}{\partial \mathbf{x}\partial \mathbf{x}^\top} &= \begin{bmatrix} \mathtt{diag}(\mathbf{b}) & \mathbf{0} \\ \mathbf{0} & \mathbf{0} \end{bmatrix} \in \mathbb{R}^{3n\times 3n} \\ \frac{\partial^2 \mathcal{U}_2}{\partial \mathbf{x}\partial \mathbf{x}^\top} &= \begin{bmatrix} \mathbf{L}_{\mathsf{BB}} & \mathbf{L}_{\mathsf{BU}} \\ \mathbf{L}_{\mathsf{UB}} & \mathbf{L}_{\mathsf{UU}} \end{bmatrix} = \mathbf{L} \in \mathbb{R}^{3n\times 3n} \\ \frac{\partial^2 \mathcal{U}_1}{\partial \mathbf{b}\partial \mathbf{x}^\top} &= \begin{bmatrix} \widehat{\Delta \mathbf{x}^{\mathsf{B}}_{t+1}} \\ \mathbf{0} \end{bmatrix} \in \mathbb{R}^{3n\times m} \\ \frac{\partial^2 \mathcal{U}_2}{\partial \mathbf{b}\partial \mathbf{x}^\top} &= \mathbf{0} \in \mathbb{R}^{3n\times m} \end{aligned} \tag{24}$$

$$
\begin{aligned}
\Delta \mathbf{x}^{\mathsf{B}}_{t+1} &= \left(\mathbf{x}^{\mathsf{B}}_{t+1} - \mathbf{x}^{\mathsf{B}}_{0}\right) \in \mathbb{R}^{3m\times 1} \\
\widehat{\Delta \mathbf{x}^{\mathsf{B}}_{t+1}} &= \sum_{i}^{m} \mathbf{e}_i \mathbf{e}_i^\top \otimes [\Delta \mathbf{x}^{\mathsf{B}}_{t+1}]_i \in \mathbb{R}^{3m\times m}
\end{aligned}
\tag{25}
$$

$\Delta \mathbf{x}^{\mathsf{B}}_{t+1}$ is the displacement of all boundary related particles from time 0 to time t. $\widehat{\Delta \mathbf{x}^{\mathsf{B}}_{t+1}}$ is a concatenated matrix of the displacement of all boundary related particles. $\mathbf{e}_i$ is the i-th column vector of the standard basis of $\mathbb{R}^m$, and $[\Delta \mathbf{x}^{\mathsf{B}}_{t+1}]_i \in \mathbb{R}^{3\times 1}$ be the deformation displacement of the i-th boundarry related particle from $\Delta \mathbf{x}^{\mathsf{B}}_{t+1}$. Note that this is the same expression from the UWD. It should be noticed that $\mathbf{L}$ is symmetric and positive semi-definite. Given these partials we get:

$$
\begin{aligned}
\frac{\partial^2 \mathcal{U}}{\partial \mathbf{b} \partial \mathbf{x}^\top} &= \frac{\partial^2 \mathcal{U}_1}{\partial \mathbf{b} \partial \mathbf{x}^\top} + \frac{\partial^2 \mathcal{U}_2}{\partial \mathbf{b} \partial \mathbf{x}^\top} \\
\frac{\partial^2 \mathcal{U}}{\partial \mathbf{x} \partial \mathbf{x}^\top} &= \frac{\partial^2 \mathcal{U}_1}{\partial \mathbf{x} \partial \mathbf{x}^\top} + \frac{\partial^2 \mathcal{U}_2}{\partial \mathbf{x} \partial \mathbf{x}^\top}
\end{aligned}
\tag{26}
$$

Substituting the above into equation 21, we get an expression for the observation jacobian:

$$
J = -\begin{bmatrix} \mathbf{L}_{\mathsf{BB}} + \mathtt{diag}(\mathbf{b}) & \mathbf{L}_{\mathsf{BU}} \\ \mathbf{L}_{\mathsf{UB}} & \mathbf{L}_{\mathsf{UU}} \end{bmatrix}^{-1} \begin{bmatrix} \widehat{\Delta \mathbf{x}^{\mathsf{B}}_{t+1}} \\ \mathbf{0} \end{bmatrix} \in \mathbb{R}^{3n\times m}
\tag{27}
$$

The first term in this expression is a function of the current boundary estimate $\mathbf{b}$, but is constant with respect to the particle states $\mathbf{x}_t$. We refer to this term as $\mathcal{R}(\mathbf{b})$:

$$
\mathcal{R}(\mathbf{b}) = -\begin{bmatrix} \mathbf{L}_{\mathsf{BB}} + \mathtt{diag}(\mathbf{b}) & \mathbf{L}_{\mathsf{BU}} \\ \mathbf{L}_{\mathsf{UB}} & \mathbf{L}_{\mathsf{UU}} \end{bmatrix}^{-1}
\tag{28}
$$

For the ease of notation we will denote that $\mathbf{D} = \begin{bmatrix} \widehat{\Delta \mathbf{x}^{\mathsf{B}}_{t+1}} & \mathbf{0} \end{bmatrix}^T$. Writing $J = \mathcal{R}(\mathbf{b})\mathbf{D}$ we can see that the jacobian given a specific boundary estimate $\mathbf{b}$ is a direct function of the displacement.

6.1.3 Boundary entropy Regarding the UWD

From section 6.1.1 and section 6.1.2, we see that to minimize entropy we have to maximize the singular values, ${\lambda_i}^2$, of $\mathcal{R}(\mathbf{b}_t)\mathbf{D}\mathbf{\Sigma}^{\frac{1}{2}}$. Where $\mathcal{R}(\mathbf{b}_t)$ is a constant given the belief at time t, and $\Sigma^{\frac{1}{2}}$ is a constant at time t.

The Frobenius norm of a matrix $\mathcal{R}(\mathbf{b}_t)\mathbf{D}\mathbf{\Sigma}^{\frac{1}{2}} = \sqrt{\sum_i^n {\lambda_i}^2}$. Thus maximizing the frobenius norm is equivalent to maximizing the magnitude of the ${\lambda_i}^2$ and decreasing entropy. Leveraging the sub-multiplicative property of the frobenius norm, the known invertibility of matrix $\mathcal{R}(\mathbf{b}_t)$, and that $\mathcal{R}(\mathbf{b}_t), \Sigma^{\frac{1}{2}}$ are constant matrices we can write:

$$
\begin{aligned}
\mathcal{R}(\mathbf{b}_t)^{-1}\mathcal{R}(\mathbf{b}_t)\mathbf{D}\mathbf{\Sigma}^{\frac{1}{2}}\mathbf{\Sigma}^{\frac{1}{2}} &\leq \mathcal{R}(\mathbf{b}_t)^{-1}\mathcal{R}(\mathbf{b}_t)\mathbf{D}\mathbf{\Sigma}^{\frac{1}{2}}\mathbf{\Sigma}^{\frac{1}{2}} \\
\mathbf{D}\mathbf{\Sigma} &\leq \mathcal{R}(\mathbf{b}_t)^{-1}\mathcal{R}(\mathbf{b}_t)\mathbf{D}\mathbf{\Sigma}^{\frac{1}{2}}\mathbf{\Sigma}^{\frac{1}{2}} \\
\frac{\mathbf{D}\mathbf{\Sigma}}{\mathcal{R}(\mathbf{b}_t)^{-1}} &\leq \mathcal{R}(\mathbf{b}_t)\mathbf{D}\mathbf{\Sigma}^{\frac{1}{2}}\mathbf{\Sigma}^{\frac{1}{2}} \\
\frac{\mathbf{D}\mathbf{\Sigma}}{\mathcal{R}(\mathbf{b}_t)^{-1}\mathbf{\Sigma}^{\frac{1}{2}}} &\leq \mathcal{R}(\mathbf{b}_t)\mathbf{D}\mathbf{\Sigma}^{\frac{1}{2}} \\
\eta\mathbf{D}\mathbf{\Sigma} &\leq \mathcal{R}(\mathbf{b}_t)\mathbf{D}\mathbf{\Sigma}^{\frac{1}{2}} \\
\eta &= \frac{1}{\mathcal{R}(\mathbf{b}_t)^{-1}\mathbf{\Sigma}^{\frac{1}{2}}}
\end{aligned}
\tag{29}
$$

Note that the Uncertainty weighted displacement (UWD) is defined as $\mathcal{D} = \mathbf{D}\mathbf{\Sigma}$.

Combining Eq. 13, Eq. 27 and Eq. 29, we show that at a given timestep t, by maximizing this lower bound $\mathbf{D}\mathbf{\Sigma}$ we can maximize $\mathcal{R}(\mathbf{b}_t)\mathbf{D}\Sigma^{\frac{1}{2}}$ and thus increase the magnitude of the singular values ${\lambda_i}^2$ and decrease entropy.

With this we have shown proposition 1: The active sensing objective of maximizing UWD is designed to decrease entropy $\mathcal{H}(\mathbf{b}_{t+1})$.

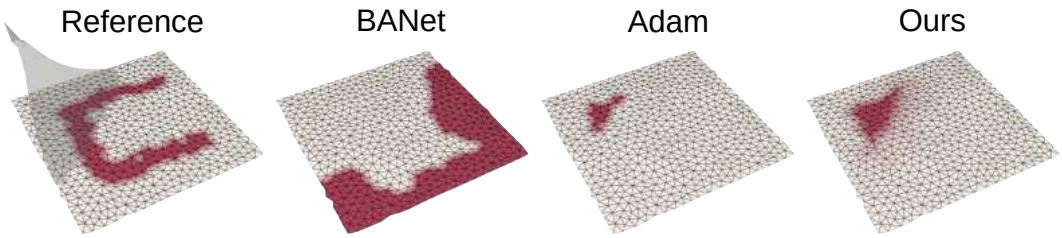

Figure 4: Estimated attachment regions of different method on test case *U-shape*. BANet is trained to estimate hard boundary conditions therefore does not generalize to our data.

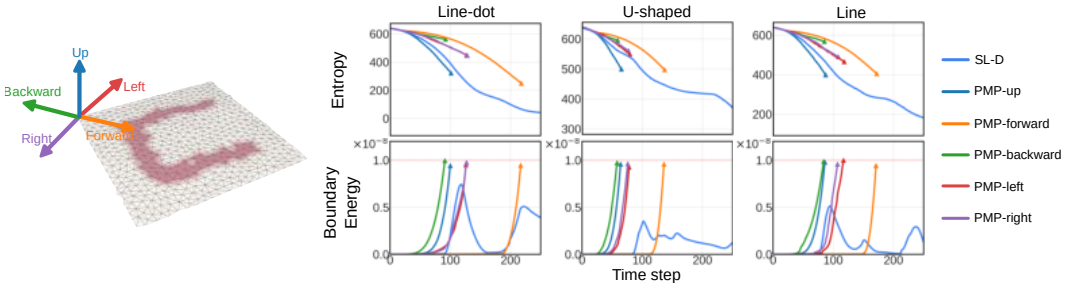

Figure 5: Additional comparison of active sensing performance between all choices of predefined motion primitives (PMP). They are *up*, *forward*, *backward*, *left*, *right*. Results from our proposed Sampling-based Large step controller (SL-D) are included for comparsion. All PMPs result in safety violation. Before violation, *up* and *forward* achieve more entropy reduction, but *up* achieves that faster in general. In comparsion, the proposed method outperform all PMPs, achieving more entropy reduction at the cost of smaller boundary energy.

6.2 Entropy loss implementation Details

In this section we discuss the implementation details for the entropy based loss from Eq. **??**. This loss is optimized in our active sensing algorithm, LG-H, to solve for the best next action.

The entropy of our belief is specified in Eq. **??** as :

$$\mathcal{H}(\mathbf{b}_{t+1}) \propto \ln\left(|\mathbf{\Sigma}_{t+1}|\right) \tag{30}$$

The ln makes directly optimizing this quantity in our loss function challenging. As uncertainty decreases and $|\mathbf{\Sigma}_{t+1}|$ approaches 0, $ln(|\mathbf{\Sigma}_{t+1}|)$ tends to $-\inf$. This makes it hard to set the weights to balance this loss with the other metrics from Eq. **??** during our unconstrained optimization.

As a result instead of directly minimizing entropy, $\mathcal{H}(\mathbf{b}_{t+1})$, we minimize the term:

$$|I - K_{t+1}J_{t+1}| \tag{31}$$

From equations Eq. **??** and Eq. 4 we get that: $\mathcal{H}(\widehat{\mathbf{b}}_{t+1}) \propto \ln\left(|(I - K_{t+1}J_{t+1})\mathbf{\Sigma}_{t+1|t}|\right)$. We can remove ln as $ln(x)$ is monotonically increasing for $x > 0$. Thus minimizing x is equivalent to minimizing $ln(x)$. $\mathbf{\Sigma}_{t+1|t}$ is a constant at the given time step and the only term we can impact with our actions is K_{t+1}. Additionally $0 \leq |I - K_{t+1}J_{t+1}| \leq 1$, making this term easier to weight in an unconstrained optimization. As a result we choose Eq. 31 in place of entropy when implementing our entropy based loss.

6.3 Additional Estimation Results

BANet [19] Adaption and Comparison. In the main text, we only compared against previous method BANet on the real world data. Here, we provide additional information about how BANet was adapted for evaluation against our framework and also show additional comparisons against BANet on simulation data.

Table 3: Additional comparison of estimation accuracy in simulated cases between BANet, the Adam optimizer, and the proposed method. Only one lift-up action is applied to all tissue because BANet only handles a single input.

	PCD ↑			PUG ↑		
Cases	BANet	Adam	Ours	BANet	Adam	Ours
Arc	10.7	75.0	100.0	37.0	5.6	14.8
Arc-line	9.4	75.0	100.0	18.2	5.5	16.4
Line	2.5	75.0	100.0	16.7	10.0	16.7
Line-dot	6.4	/	100.0	13.3	0.0	5.1
U-shape	2.3	80.0	100.0	4.8	11.5	22.1

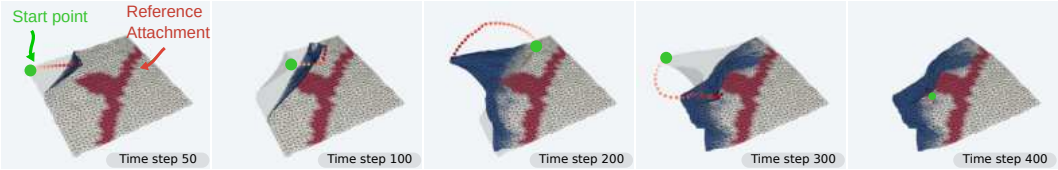

Figure 6: Active sensing performance of our framework with doubled amount of mesh particles (1200) on test cases *Line-dot*. Our framework can still perform complex maneuvers such as switching directions and flipping for informaiton gain even with more particles, showing that it can generalize to complex meshes.

BANet takes in a 3D volume representing the tissues and its deformation field at the end of each test cases as inputs. It then classifies if each voxel is boundary or not. We convert our triangular mesh to be volumetric by marking the closest voxel to each of our mesh particles to be part of the volumetric representation. The mesh's particle displacement can be calculated with our proposed method (i.e. $\mathbf{x}_{\text{end}}^{\text{ref}} - \mathbf{x}_{0}^{\text{ref}}$). A displacement field is computed by assigning the mesh particles' displacement to the closest voxel and setting the displacement everywhere else to be zero. We assign the threshold to be small (0.1) to include more relatively low-scored results from BANet because it assumes hard boundary conditions whereas our scenarios do not rely on that specific assumption. Lastly, boundary condition of mesh particles are determined by checking the BANet outputs corresponding to their closest voxel.

Additional comparisons between our method and BANet are shown in Table 3. Looking at the PCD metric, BANet predicts inaccurate results. Fig. 4 explanins it by showing that BANet tends to regard not-displaced particles as boundaries. In fact, if we increase the binary threshold to 0.5, BANet predicts few boundary conditions. Note that this is correct for BANet because it assumes hard boundary conditions in its training data whereas in our test cases there is no hard boundary condition. But it also showed that BANet does not generalize to our attachment scenario that is common in surgery.

6.4 Additional Active Sensing Results

Motion Primitive Details. We show additional details from the experiment discussed in the paper when comparing our method with the motion primitives in [15]. Due to ground contact, moving downward is forbidden. Therefore, we only consider 5 motion primitives of *up*, forward, *backward*, *left*, and *right*. There direction w.r.t to the tissue is shown in the left of Fig. 5. To avoid sliding, all primitives are preceeded by a grasp sequence that lifts up the tissue. Fig. 5 shows additional comparison between the proposed method and all choices of predefined motion primitives (PMP). All PMPs result in safety violation. Before violations, *up* and *forward* achieve more entropy reduction, but *up* achieves that faster in general. In comparsion, our proposed method outperforms all PMPs, achieving more entropy reduction at the cost of smaller boundary energy.

6.5 Scalability

We evaluate our framework's ability to handle higher dimensional meshes. This become important when simulating surgical scenes of higher complexity. Specifically, we double the number of par-

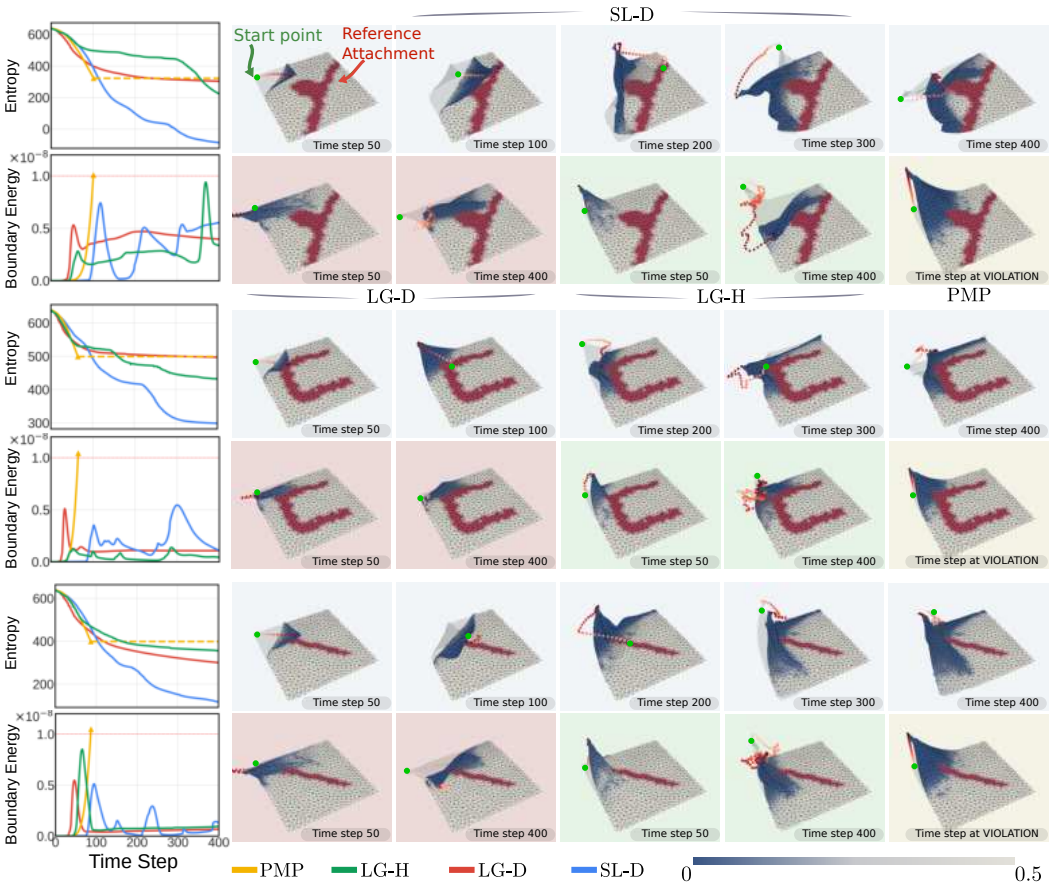

Figure 7: Results from our active sensing experiments with 4 different strategies: PMP (yellow) is a baseline, and SL-D (blue), LG-H (green), and LG-D (red) are proposed in this work. Every two rows show one experiment with the entropy and energy plotted in the left-most column, and the images on the right show a collage of the control trajectories being applied from the different active sensing strategies. Note that the colored background on each image corresponds to the active sensing strategy (best viewed in color). The red color on the tissue highlights the reference attachment, and the blue shows the confidence, inverse of variance, of the estimated boundary. The goal of the active sensing strategies is to maximize the confidence, which is measured in entropy, while adhering to safety constraints, which are measured in energy. Overall, SL-D achieves more entropy reduction than all other baselines while keeping a safe boundary energy profile. It also produces the most intricate control point trajectories, such as switching directions and folding. In comparison, local controllers LG-H and LG-D get trapped in local minima, resulting in higher entropy. PMP reduces entropy in the beginning but results in quick safety violations.

ticles on our mesh (1200 particles). We show the performance of our framework with our most computation-demanding task, active sensing, in Fig. 6. Our framework is able to maintain the similar amount of information gain with more particles. The computation time of our active sensing controller increases from 2.9s to 4.5s. Despite increase in computation time, we believe our algorithm can be accelerated via techniques such as asynchronous computation and multi-resolution meshes to handle more complex scenarios.

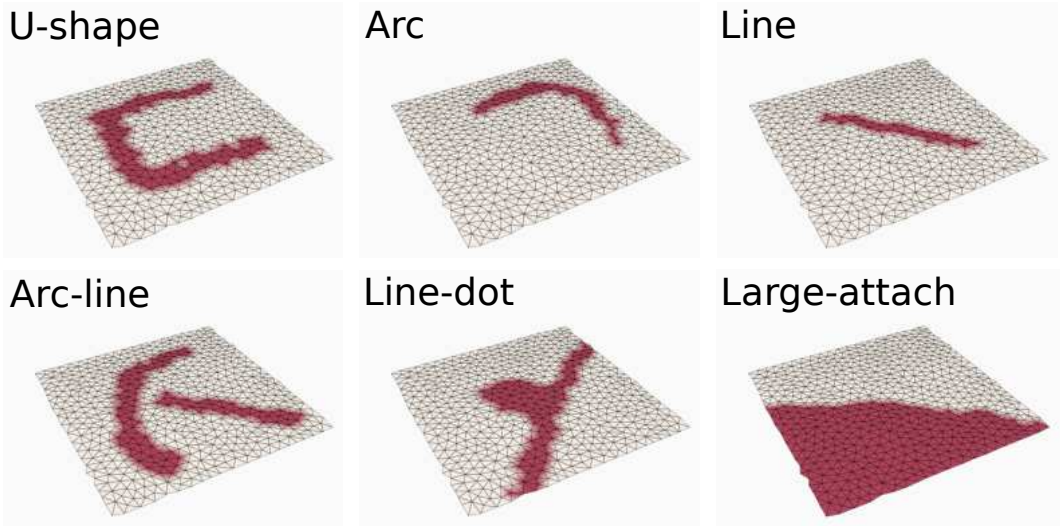

Figure 8: The images show the ground truth attachment points in red using spring boundary constraints for the simulation test cases in our experiments.

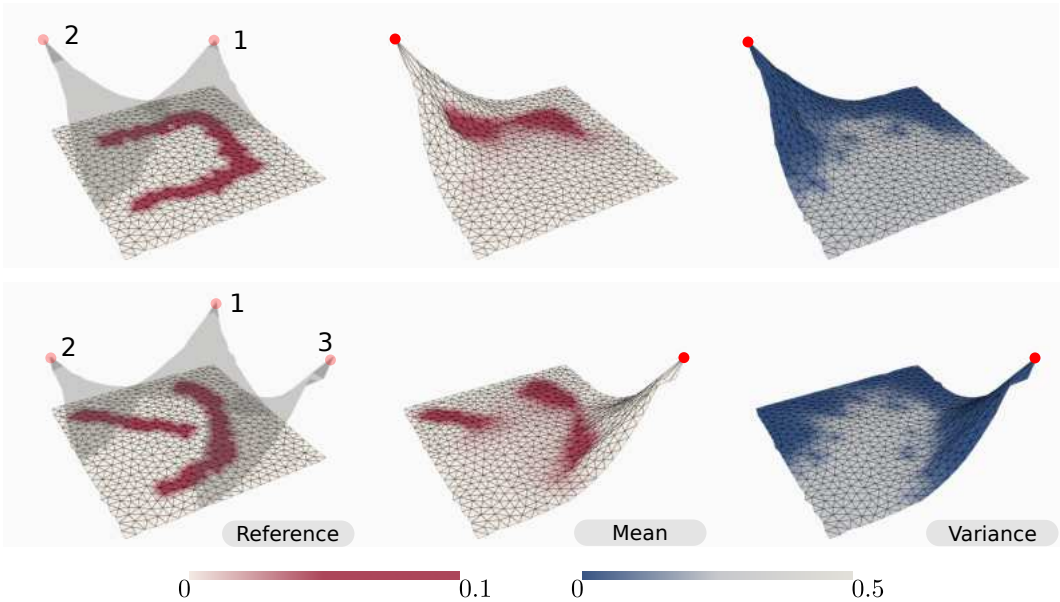

Figure 9: Example results from our estimation framework on simulated environments where the order of the grasps is numbered, and the boundary is highlighted in red on the left-most column. The final result from our proposed method is shown in red in the middle column. Finally, the confidence (inverse of variance) of our estimation is shown in blue in the rightmost column. We can see how the variance has decreased in the regions where the trajectories have displaced the tissue from its original state, and the mean estimate has converged close to the reference values.

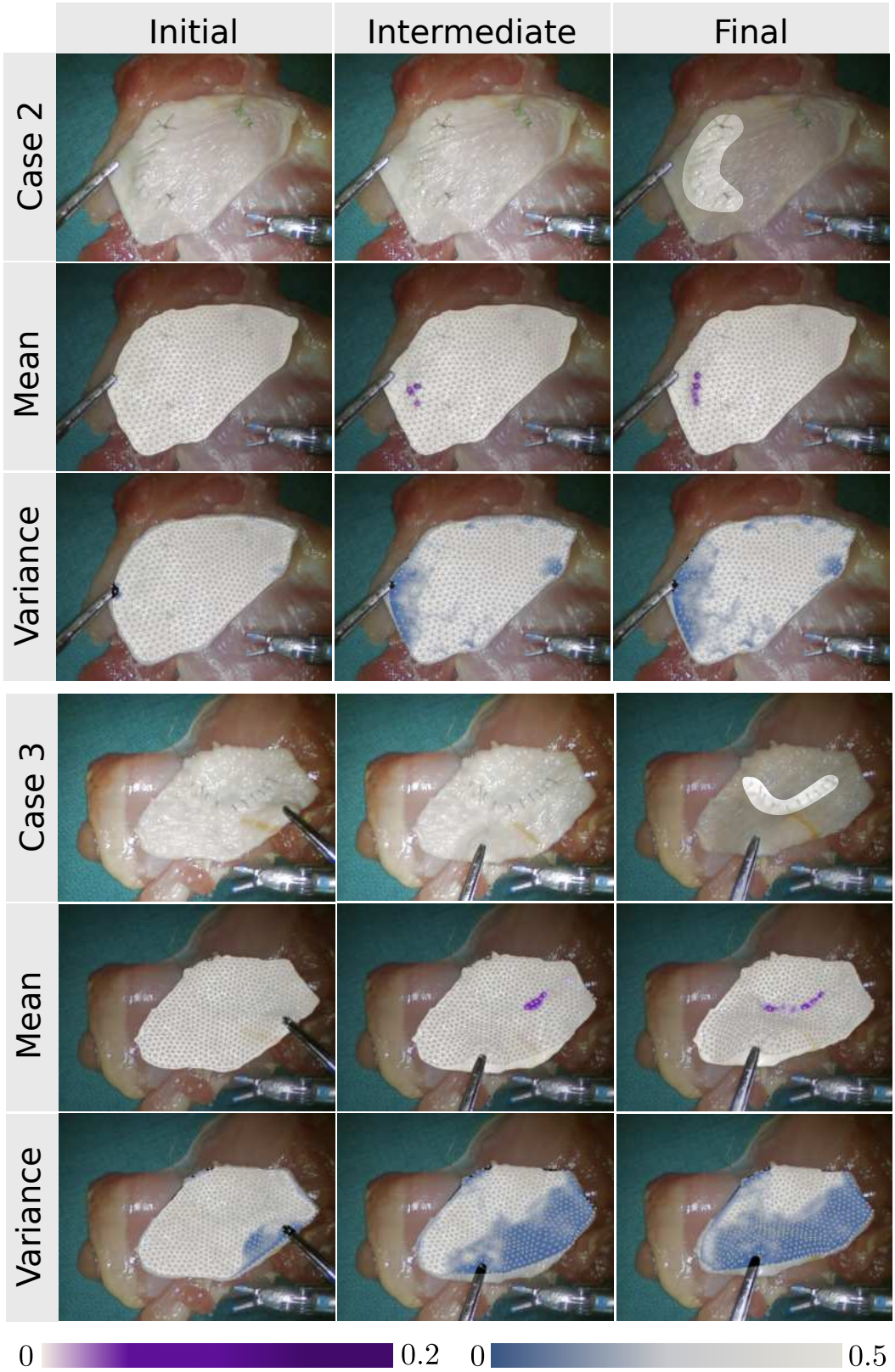

Figure 10: This figure shows results from real-world tissue attachment point estimation experiments case 2 and case 3 (case 1 is shown in Fig. 1). Time progresses from left to right. A dark purple value corresponds to a stronger estimated attachment point, and a darker blue value corresponds to lower uncertainty about the boundary parameters at that region. Notice that as the tissue is deformed, the variance decreases, and the estimated mean of our boundary matches closer to the ground truth.

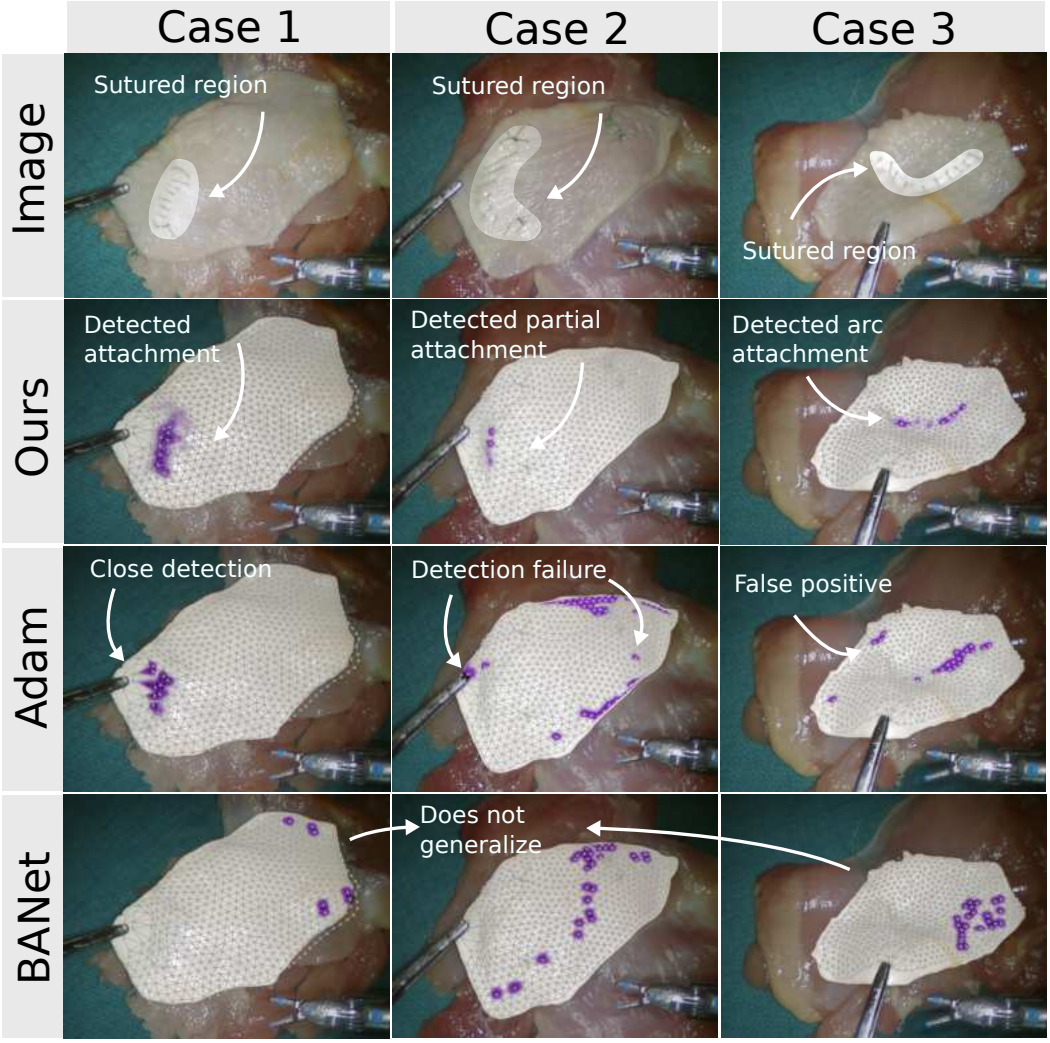

Figure 11: Detailed comparison of estimated attachment points between the proposed method and the Adam optimizer. In the second row, our method successfully detects attachment shape. In comparison, the Adam optimizer estimates predictions that are close to the true region (case 1) but fails in other cases, producing many false positive estimations. Because BANet cannot generalize to our real-world data, it fails to predict meaningful results.

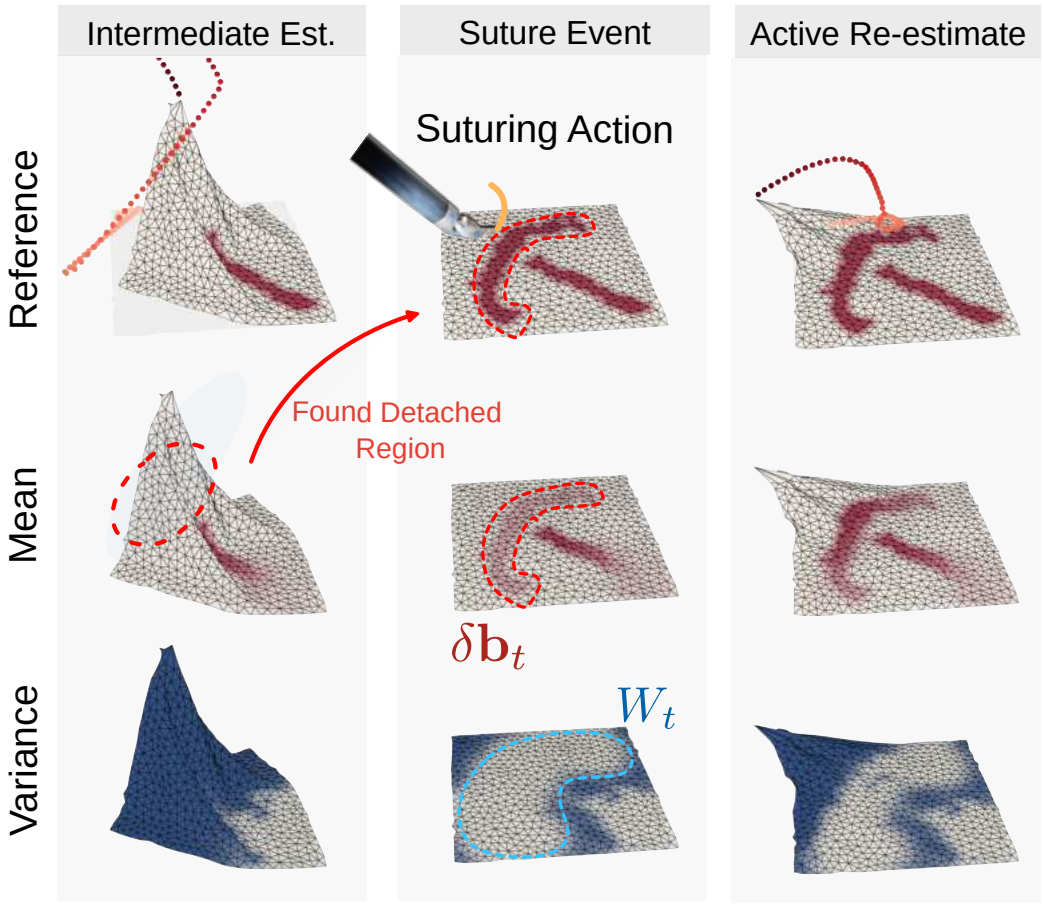

Figure 12: We applied JIGGLE to a suturing procedure by 1) the left column: applying the active sensing approach to find where the tissue is detached, 2) the middle column: applying a suture action at the desired detached area, and 3) the right column: active sensing again to validate the suture action. The top row of images shows the ground truth attachment in red, and the bottom row shows our estimation of the boundary in red and the confidence, inverse of variance, in blue. After each suture is applied, the suture information is also fed into our estimation algorithm, including a noise injection near the suture region, so the active sensing policy is encouraged to confirm where the new boundary has been added. The second re-estimation, confirming the boundary after the suture, reports an increase in PUG from 20.2 to 75.2. The PCD value remains the same at 100, indicating no false detections.

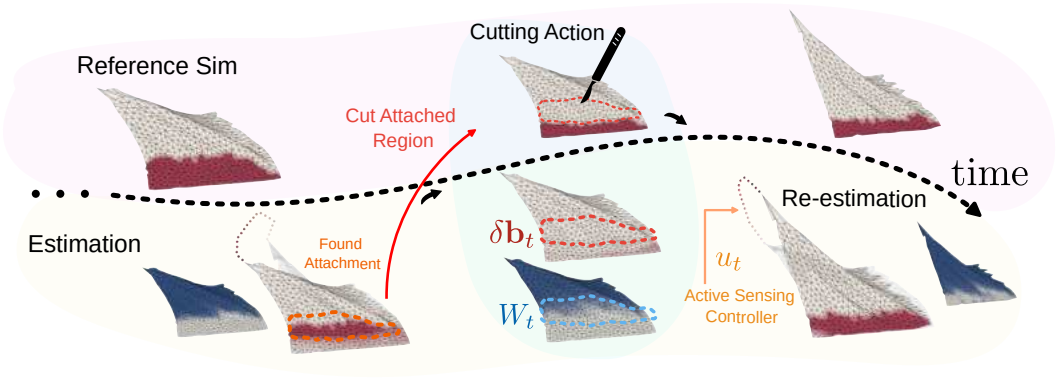

Figure 13: We applied JIGGLE to a tissue detachment procedure on test case *Large-attach*, which is done by iteratively applying the active sensing approach to find the attachment points, and then a cut is made at that discovered boundary. The sequence of images depicts an iteration of this procedure where the top row shows the ground-truth boundary attachment in red, and the bottom row shows our estimation of the boundary in red and the confidence, inverse of variance, in blue. After each cut action is applied, where all of the discovered boundary is removed, the cutting information, $\delta \mathbf{b}_t, W_t$, is also fed into our estimation algorithm. The strategy is repeated until the tissue is fully detached and it took 7 cycles in this experiment to detach the tissue successfully .